PROSTHETICS

Closed-loop optogenetic neuromodulation enables high-fidelity fatigue-resistant muscle control

Guillermo Herrera-Arcos[1,2,3], Hyungeun Song[1,4], Seong Ho Yeon[1,2], Omkar Ghenand[1,5], Samantha Gutierrez-Arango[1,2], Sapna Sinha[1,3], Hugh Herr[1,3]*

Closed-loop neuroprostheses show promise in restoring motion in individuals with neurological conditions. However, conventional activation strategies based on functional electrical stimulation (FES) fail to accurately modulate muscle force and exhibit rapid fatigue because of their unphysiological recruitment mechanism. Here, we present a closed-loop control framework that leverages physiological force modulation under functional optogenetic stimulation (FOS) to enable high-fidelity muscle control for extended periods of time (>60 minutes) in vivo. We first uncovered the force modulation characteristic of FOS, showing more physiological recruitment and significantly higher modulation ranges (>320%) compared with FES. Second, we developed a neuromuscular model that accurately describes the highly nonlinear dynamics of optogenetically stimulated muscle. Third, on the basis of the optogenetic model, we demonstrated real-time control of muscle force with improved performance and fatigue resistance compared with FES. This work lays the foundation for fatigue-resistant neuroprostheses and optogenetically controlled biohybrid robots with high-fidelity force modulation.

INTRODUCTION

Skeletal muscles are biological actuators responsible for almost all movement in animals and humans. Since Luigi Galvani's experiments of muscle contraction via electrical stimulation of motor axons, scientists have developed means to understand and probe muscles to generate controlled motion. In various neurological conditions, the communication pathway between the central nervous system and neuromuscular components is severed, resulting in motor deficits such as paralysis. Neuroprostheses can replace the missing neuronal input by delivering precise commands using artificial stimulation to restore muscle function. Functional electrical stimulation (FES) has been the dominant stimulation modality. Understanding of the relationships between stimulation parameters and muscle behavior (*1*, *2*), the nonlinear recruitment characteristic (*1*, *3*, *4*), and spatiotemporal properties of FES-stimulated muscles (*1*, *4*–*7*) has enabled the development of numerous models (*1*, *3*, *8*–*11*) and closed-loop demonstrations. For example, grasping has been restored in nonhuman primates (*12*) and humans with tetraplegia (*13*, *14*), walking speeds (*15*, *16*) and muscle structural changes (*17*) have been improved in patients with drop foot, and control over diaphragm function has been restored using phrenic nerve stimulation in patients with spinal cord injury and amyotrophic lateral sclerosis (*18*).

Despite substantial advancements, FES is characterized by reverse recruitment order of motor units, where large fatigable units are recruited before smaller fatigue-resistant units (*19*). This is contrary to the way the central nervous system recruits motor units (orderly recruitment), where small motor units are recruited first for low-force fine motor control and larger units are recruited with increasing levels of motor activation for high-force activities (*20*, *21*). The reverse recruitment mechanism of FES makes fine-force modulation challenging (*2*, *22*) and fatigues muscles after a few minutes of stimulation (*19*, *23*, *24*). Thus, the field requires a new stimulation modality that can provide reliable, long-term, graded muscle modulation for chronic rehabilitation applications such as full restoration of dexterous grasping.

Recently, functional optogenetic stimulation (FOS) (*25*), a technology that uses light to artificially stimulate genetically modified nerve cells (*26*), has enabled orderly recruitment of motor units as shown by axon latency metrics (*19*). This suggests that FOS could serve as neuromodulation strategy for motor prostheses. However, the relationship between stimulation parameters and force production that would inform optogenetic modulation strategies, as well as the force modulation characteristic of FOS, remains unknown. These shortcomings have precluded the development of biophysical models that could be leveraged in closed-loop neuroprostheses to achieve accurate and fatigue-resistant muscle control.

We hypothesized that FOS would enable high-fidelity and fatigue-resistant control of muscle force, conferred by a more physiological force modulation mechanism, compared with FES. To address this hypothesis, we conducted three experiments where metrics of force modulation and control performance were directly compared between FOS and FES. We first performed open-loop stimulation protocols to mechanistically characterize the force modulation characteristic. Then, muscles were stimulated using dynamically rich signals to perform system identification procedures for biophysical modeling. Last, the biophysical model was used to design a closed-loop controller, and its performance was evaluated over short and extended durations (Fig. 1A). These results provide a comprehensive characterization of FOS muscle dynamics, elucidating neuromodulation strategies to orchestrate motor recruitment, enabling the development of an optogenetically stimulated muscle model and demonstration of accurate fatigue-resistant muscle control (Movie 1). This work lays the foundation for neural controllers for optogenetically modulated motor prostheses.

RESULTS

Spatiotemporal stimulation protocols for muscle characterization

To comprehensively characterize muscle dynamics and perform closed-loop muscle control in vivo, we developed a platform capable of repeatable and accurate sensing and stimulation. The platform

[1]K. Lisa Yang Center for Bionics, MIT, Cambridge, MA, USA. [2]Program in Media Arts and Sciences, MIT Media Lab, Cambridge, MA, USA. [3]McGovern Institute for Brain Research, MIT, Cambridge, MA, USA. [4]Harvard-MIT Division of Health Sciences and Technology (HST), MIT, Cambridge, MA, USA. [5]Department of Biological Engineering, MIT, Cambridge, MA, USA.
*Corresponding author. Email: hherr@media.mit.edu

comprises an adjustable muscle characterization apparatus (Fig. 1B) capable of high-resolution muscle force recordings (Fig. 1C and fig. S1), electromyographic (EMG) recordings, and precise optical and electrical stimulation along the nerve (fig. S2). Neural stimulation (FOS or FES) was delivered to the tibial nerves of anesthetized transgenic mice expressing the excitatory opsin channelrhodopsin-2 (ChR2) under the *Thy1* promoter (*19*), whereas force and EMG were recorded from the lateral gastrocnemius. Detailed descriptions of the surgical and experimental procedures can be found in Materials and Methods.

To elucidate the spatial behavior of FOS, stimulation was delivered to a proximal and distal location of the nerve (fig. S3A). The force dynamics at the proximal stimulation location exhibited a pronounced force decay after an initial peak before decaying to a steady state. In some cases, steady state was not achieved, and just the initial peak was observed. In contrast, force dynamics at the distal location showed a less pronounced force decay, indicating sustained force generation and distinct steady-state values (fig. S3C). Recruitment curves in fig. S3D showed higher steady-state force values (distal: 138.5 mN; proximal: 33.6 mN) and higher force resolution between stimulation pulses (distal: 12.5 mN; proximal: 2.9 mN) under distal compared with proximal stimulation. This was not observed with FES (fig. S3B). Immunohistochemical analysis suggested that this proximodistal behavior of FOS is not related to different ChR2 channel expression levels along the nerve (fig. S4). On the basis of this result, stimulation on subsequent experiments was delivered to the distal section of the nerve. Stimulation pulses were 2 s to ensure that steady-state force was achieved, with at least 25 s of rest between consecutive pulses to avoid fatigue (*1*). No fatigue was observed as illustrated by the monotonic shape of the recruitment curves. The stimulation protocol is described in more detail in Materials and Methods.

Given the extended duration of the stimulation pulses, we observed steady-state force responses following distinct dynamics between stimulation modalities. For FOS, after reaching peak force, there was a force decay before reaching steady state. These dynamics closely resemble the desensitization to a smaller steady-state conductance observed in ChR2 whole-cell patch-clamp studies (*27*). For FES, the initial force decay after peak force was less prominent than that for FOS, achieving steady state earlier and at higher levels (Fig. 1C). Similar dynamics and magnitudes have been observed in previous optogenetic studies in rodents (*19*, *28*).

Optogenetic force modulation

Muscle force can be modulated via two main mechanisms: motor unit recruitment and rate coding (*29*). Motor unit recruitment is achieved by varying the number of motor units that are active, whereas rate coding is achieved by varying the firing rate of individual motor units because of greater overlap of successive muscle twitches. Steady-state responses were sought because twitch responses may be different

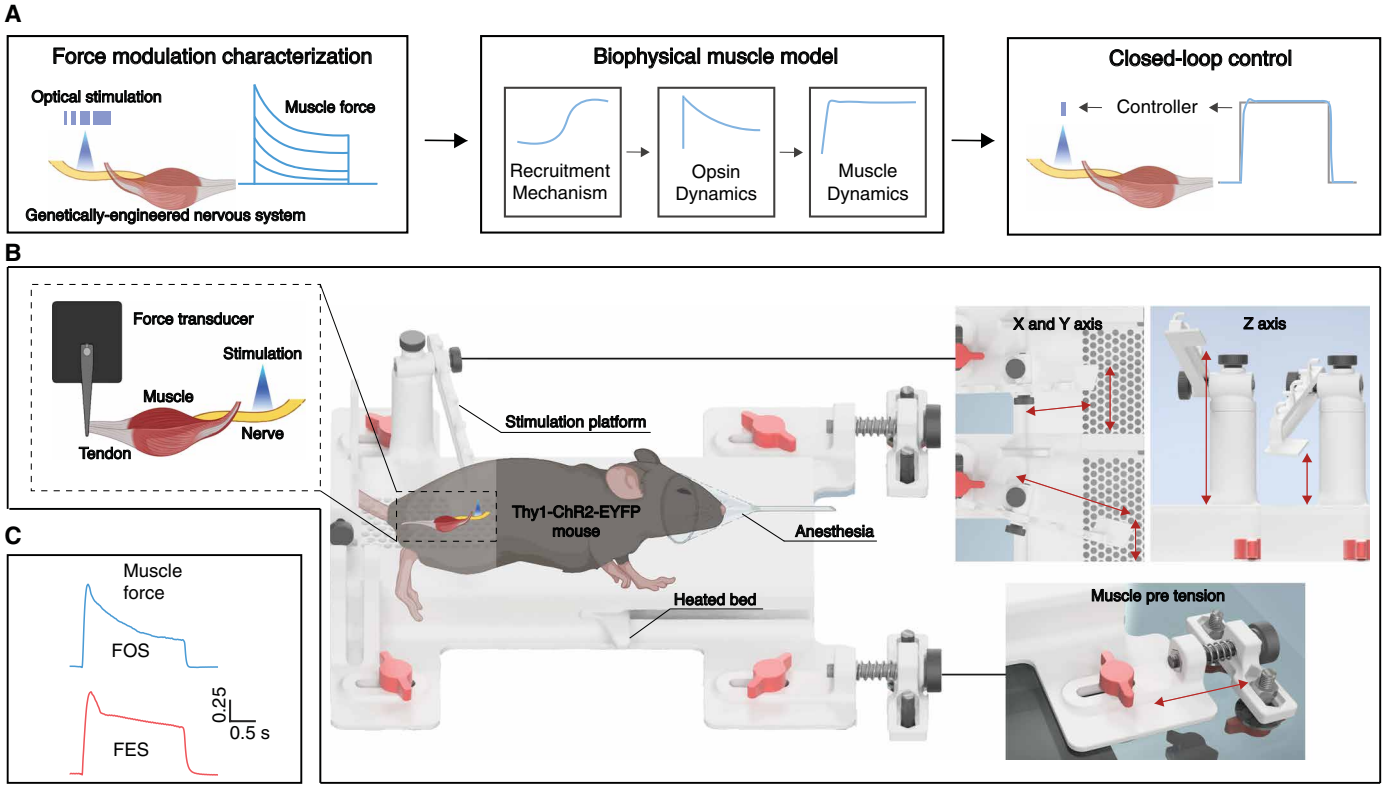

Fig. 1. Experimental framework for muscle characterization and control. (**A**) Stimulation protocols were performed to characterize the muscle force modulation and, together with dynamically-rich stimulation signals, to develop a biophysical muscle model; last, the biophysical muscle model was used to design a controller for closed-loop force modulation. (**B**) 3D render of the muscle characterization apparatus comprising a heated bed for in vivo experimentation in rodents, an adjustable platform for optical and electrical stimulation, and an adjustable force recording platform, with close-up views of the three degrees of freedom (DOF) of the stimulation platform and the three DOF of the force recording platform comprising a force transducer and a muscle pretensioner. (**C**) Example of acquired muscle force signals under FOS and FES.

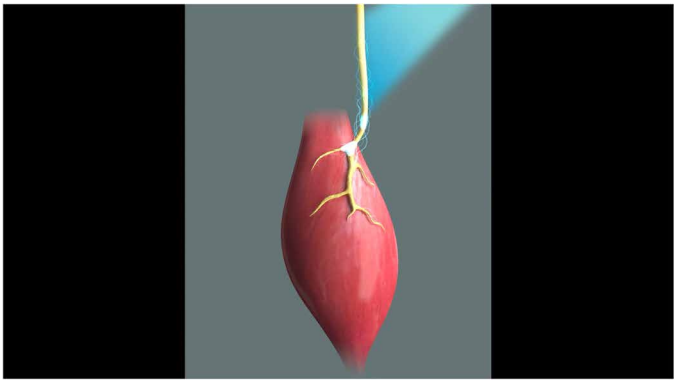

Movie 1. Overview of optogenetic system for high-fidelity and fatigue-resistant muscle control.

from the control signals typically used in neuroprosthetic control. Aimed at quantifying graded muscle modulation, we constructed muscle recruitment curves. The recruitment curve of a muscle is a measure of the number of active muscle fibers (*4*) and can be defined as the input-output relationship between stimulus activation level and muscle force (*1*, *4*). The shape of this relationship determines the degree of proportionality that can be achieved (*4*) and is thought to be recruitment order dependent (*29*). Therefore, a more gradual force modulation is a sign of orderly recruitment (*30*).

To vary the number of recruited motor units, we used pulse width modulation adjusted to the maximum muscle force range (see Materials and Methods). We observed fundamentally different recruitment curves between FOS and FES (Fig. 2A). The FES recruitment curve showed close to all of the muscle force (80.4%) generated at low stimulation values (pulse width: 33.33%). Contrarily, the FOS recruitment curve showed low force production (40.3%) at the same stimulation value (Fig. 2A), indicating excitability threshold differences between the stimulation modalities. The recruitment slope between 0 and 75% of muscle force was significantly smaller for FOS compared with FES (fig. S5A), indicating that, under FES, fibers responsible for high force production are recruited first, whereas under FOS, fibers can be recruited to generate force from small to large, proportionally to the stimulation command, to generate a more graded force modulation. Comparison of the modulation range to generate 25 and 50% of muscle force revealed significantly higher resolution for FOS compared with FES (fig. S5B) and across the whole muscle force range (fig. S6A and table S1). At 25 and 50% of force, FOS had a modulation range 324 and 390% higher than FES. Moreover, the modulation range required to go from 25 to 50% of muscle force was significantly different for FOS (25% of force: 27.0%, 50% of force: 36.3%; fig. S5B and table S1), whereas for FES, it remained at a similar range (25% of force: 8.3%, 50% of force: 9.3%; fig. S5B and table S1). Previous studies have shown the FES recruitment curve to be highly nonlinear (*1*, *3*, *4*); the nonlinear shape is dictated by the location and size distributions of the individual motor unit axons within the nerve, with large-diameter axons having a lower stimulation threshold than small-diameter axons (*1*). A quantitative nonlinearity analysis of the recruitment profiles (see Materials and Methods for definition of

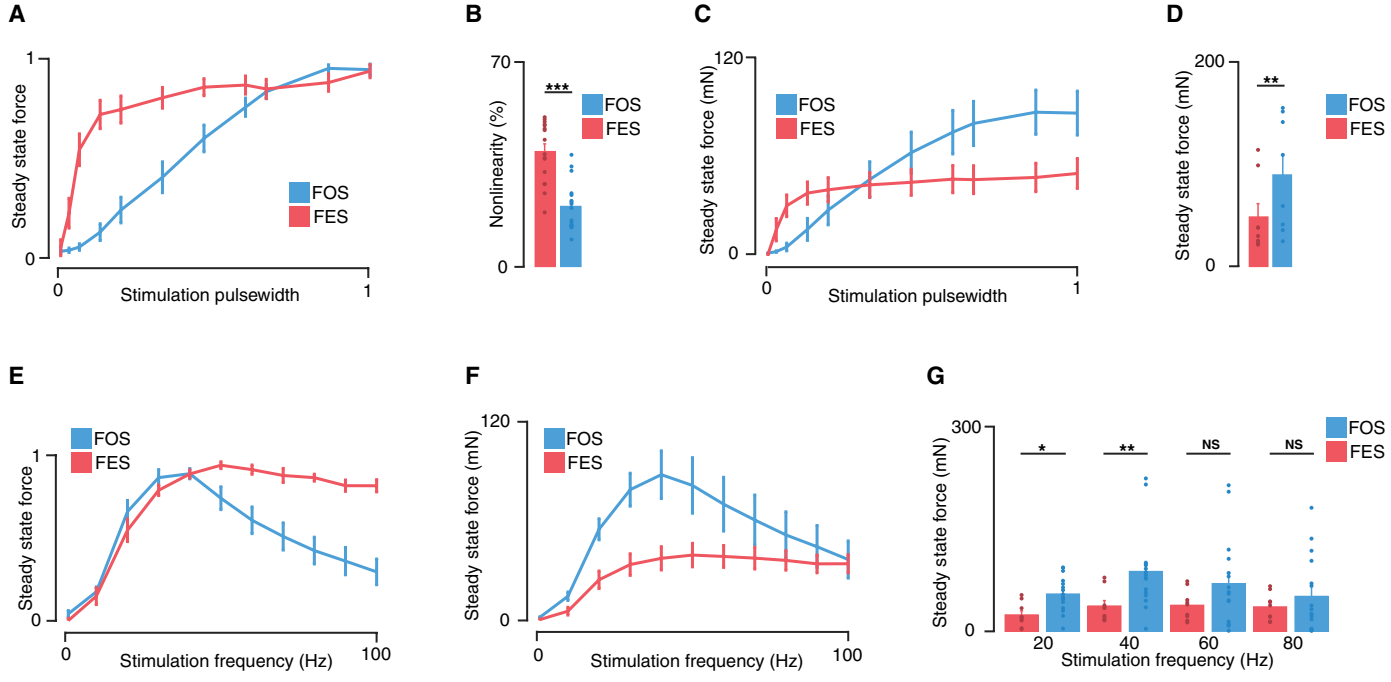

Fig. 2. Optogenetic force modulation. (**A**) Normalized steady-state force versus stimulation pulse width under FOS and FES. Stimulation frequency is 60 Hz, and stimulation amplitude is one that generates 33% of maximal force ($n = 8$). (**B**) Nonlinearity measure for FOS and FES ($n = 8$); $^{***}P < 0.005$. (**C**) Steady-state force versus stimulation pulse width ($n = 8$). (**D**) Steady-state force at maximum stimulation for FOS and FES ($n = 8$); $^{**}P = 0.0098$. (**E**) Normalized steady-state force versus stimulation frequency ($n = 8$). (**F**) Steady-state force versus stimulation frequency ($n = 8$). (**G**) Steady-state force for FOS and FES at 20, 40, 60, and 100 Hz ($n = 8$); $^{*}P = 0.0192$; $^{**}P = 0.0053$; NS, not significant. For additional statistical analysis details, see table S3. $^{***}P < 0.005$; $^{**}P < 0.01$; $^{*}P < 0.05$; NS, not significant. Paired two-tailed *t* test at significance level ($\alpha = 0.05$). Error bars represent SEM.

nonlinearity measure) (*31*) indicated that the FES recruitment curve was significantly more nonlinear than FOS (FES: 39.39%, FOS: 20.63%; Fig. 2B). To further describe this, we constructed recruitment curves on the basis of integrated EMG, as a proxy for volitional neural signals (fig. S6B). We again found that FOS had higher modulation ranges across the whole muscle force range compared with FES (fig. S6C and table S2). This suggests that FOS is able to precisely modulate the activation of both small and large motor units.

We found that FOS generated higher steady-state force at around half-maximal and significantly higher force at maximum stimulation when compared with FES (FOS: 89.7 mN, FES: 48.6 mN; Fig. 2, C and D). FOS generated higher peak force across the whole stimulation range (fig. S6D) and significantly higher force at maximum stimulation compared with FES (FOS: 252.5 mN, FES: 83.2 mN; fig. S6E). This suggests that FOS can activate motor units that are inaccessible to FES, although only a portion of motor units may be genetically transduced (fig. S4) (*28*).

We next examined rate coding of FOS. To vary the firing rate of individual motor units, we used frequency modulation adjusted to the maximum muscle force range (see Materials and Methods). Although motor unit recruitment is usually preferred over a moderate force range because of the fatigue effects at high frequencies (*3*), it presents another strategy for force modulation. Similarly to FES, under FOS, we observed modulation of force as stimulation frequency increased up to 40 Hz. However, after 40 Hz, steady-state force under FOS started to decrease, whereas under FES, force was maintained (Fig. 2E). Previous optogenetic studies have shown a frequency limit related to opsin kinetics attributed to a desensitization of ChR2, suggesting that opsins with faster kinetics may be used to overcome this (*28*). In a study with viral-mediated ChR2, it was found that activations greater than 36 Hz resulted in a reduction in force (*28*). In a study in nonhuman primates, EMG responses tracked FOS up to 16 Hz (*32*). We found a frequency limit for excitatory opsin ChR2 to be around 40 Hz in our study (Fig. 2E). We then asked whether this limits the absolute force magnitude that can be achieved. Steady-state force was significantly higher for up to 50 Hz, where for higher frequencies (60 to 100 Hz), similar values were observed compared with FES (Fig. 2, F and G, and table S3). Peak force was also significantly higher for all frequencies compared with FES (fig. S6, F and G, and table S4). This suggests that although the FOS frequency range for force modulation is smaller, the force that can be achieved is higher at low frequencies and similar at high frequencies compared with FES. These data showed that FOS activation achieved proportional, graded, and more linear force modulation, as well as similar or higher muscle force production compared with FES, opening the possibility of repeatable and precise muscle control.

Biophysical optogenetically stimulated muscle model

We leveraged the aforementioned force modulation to develop a biophysical model of optogenetically stimulated muscle. Artificially stimulated muscles exhibit a number of nonlinear dynamics because of the recruitment mechanism and muscle dynamics. In addition, the force dynamics of FOS are highly nonlinear because of the opsin kinetics effect on the exponential force decay dynamics (fig. S7). Although we have noted that the FOS recruitment characteristic is more physiological and follows a more linear relationship than FES (Fig. 2B), it was considered nonlinear because muscle length-tension properties (*1*) and movement of stimulating electrodes (*4*) might contribute to nonlinear behavior beyond the number of active motor units (recruitment). Hence, we aimed at modeling optogenetically stimulated muscles using nonlinear identification procedures used on other biological systems, such as retinal neural processing (*33*), neural responses of bullfrogs (*34*), and dynamics of FES-stimulated muscle (*1*, *3*). The model comprised a static nonlinearity representing the recruitment mechanism, a dynamic system representing the opsin dynamics, and a linear dynamic system representing the muscle dynamics (Fig. 3A).

Logistic fitting was used to model the recruitment characteristic for both FOS and FES; however, the parameters between them significantly differed. From the logistic function equation (Eq. 1), we compared two parameters that describe the shape of the function: Recruitment steepness describes the slope or growth rate (γ), and large fiber activation threshold describes the midpoint between the peak and baseline (δ). We found the recruitment steepness for FOS to be significantly smaller than FES (FOS: 1.0, FES: 7.0; Fig. 3C), indicating more proportional and graded recruitment of FOS than FES. We observed the large fiber activation threshold for FOS to be significantly higher than FES (FOS: 5.9, FES: 1.2; Fig. 3D), suggesting that FOS has a higher threshold for large fiber activation compared with FES.

$$f_R(u) = \beta \frac{1}{1 + e^{-\gamma(u-\delta)}} \tag{1}$$

Muscle dynamics were modeled as a continuous-time linear second-order system comprising muscle activation and muscle-tendon force dynamics. It has been shown that under isometric conditions, the forces produced by muscles in cats and humans in response to randomly applied inputs can be sufficiently approximated by linear dynamic models (*2*, *3*, *22*, *35*). We modeled activation dynamics and used a linear muscle-tendon force dynamic model (*36*), resulting in the muscle-tendon force dynamics in Eq. 2. G_F is a muscle activation coefficient, k_T is a parallel tendon elasticity element, b_T is a parallel tendon viscosity element, k_M is a parallel muscle elasticity element, b_M is a parallel muscle viscosity element, s is the variable in the frequency domain, and A is the muscle activation (see Materials and Methods for detailed model derivation).

$$F_{MT}(s) = \frac{G_F(k_T + b_T s)}{(k_M + k_T) + (b_M + b_T)s} A \tag{2}$$

The FOS force decay is the predominant difference between FOS and FES dynamics. We hypothesized that an extra block with exponential dynamics representing the effect of opsin kinetics on force dynamics could account for this difference. To validate this, FOS force dynamics were fitted to an exponential function (Fig. 3E). Across stimulation values (Fig. 3F, top) and stimulation durations (Fig. 3F, bottom), the coefficient was found to be constant, indicating that an exponential dynamics block is suited to account for the decaying FOS force dynamics. The variability between animals could be explained by the difference in the number of motor units expressing the opsin, different expression levels (*25*, *37*), and slight changes in optical illumination.

On the basis of the proposed model, a system identification procedure for Hammerstein architectures was used (fig. S8) (*38*). Pseudo-random binary signals at different stimulation levels were used as input, and muscle force was recorded as the output. A portion of the data (70%) was used for the identification procedure, and

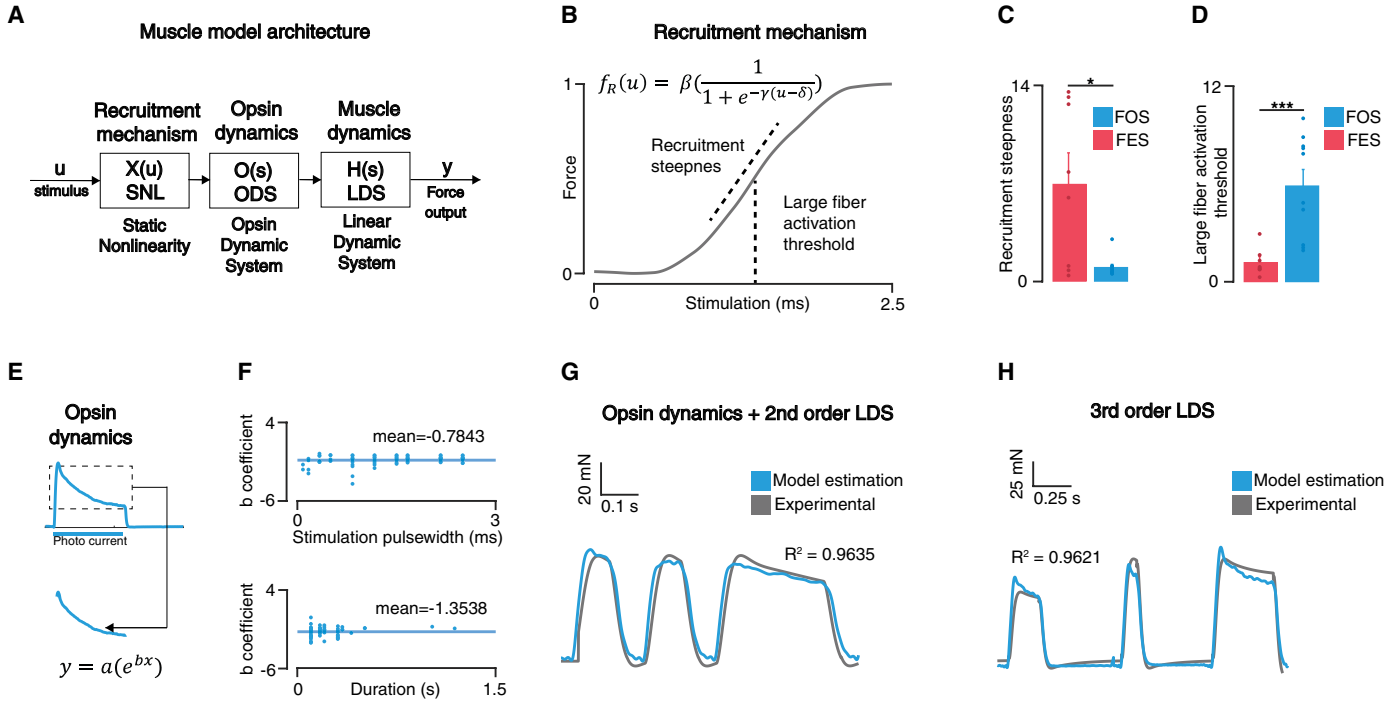

Fig. 3. Optogenetically stimulated muscle model. (**A**) Model architecture for FOS comprising static nonlinearity (SNL), opsin dynamic system (ODS), and linear dynamics system (LDS). X(u) refers to a static nonlinearity that is a function of stimulation "u," O(s) and H(s) refer to the transfer function of dynamic systems in the frequency domain "s." (**B**) Logistic fitting of muscle recruitment curve. (**C**) Recruitment steepness comparison between FOS and FES recruitment curves ($n = 5$); $^*P = 0.0189$. (**D**) Large fiber activation threshold comparison between FOS and FES recruitment curves ($n = 5$); $^{***}P < 0.005$. (**E**) Exponential fitting of decaying force dynamics under FOS. (**F**) Exponential coefficient at different stimulation pulse width values (top) and stimulation durations (bottom) ($n = 5$). (**G**) Estimation and experimental force dynamics using a second-order LDS with opsin dynamics model architecture. (**H**) Estimation and experimental force dynamics using a third-order LDS model architecture. $^{***}P < 0.005$; $^*P < 0.05$. Paired two-tailed t test at significance level ($\alpha = 0.05$). Error bars represent SEM.

the remaining 30% was used to evaluate its performance. After the system identification procedure converged (no change in root mean square error between measured and estimated force values for 10 runs), for FOS, the opsin dynamics were added. A representative trial of the estimated FOS force dynamics showed that estimated dynamics closely replicated experimental dynamics (Fig. 3G). The model performance was evaluated by measuring the correlation between estimated and experimental values, showing that the model accurately depicted muscle dynamics of FOS ($R^2 = 0.9635$; fig. S9). The model performance for the rest of the animals also showed similar performance ($R^2 = 0.9447$; $n = 3$; fig. S9). For FES, no additional dynamics were added. The model performance for FES showed accurate replication of experimental muscle dynamics ($R^2 = 0.9221$; $n = 3$; fig. S9). As expected, the muscle dynamics were similar between FOS and FES; the distinction in force dynamics stemmed from the recruitment mechanism and opsin dynamics (fig. S10).

We aimed to use the model for closed-loop muscle control; however, it is challenging to obtain an inverse of the opsin dynamic system because of its nonlinear characteristic. A second-order linear system was insufficient to capture FOS dynamics (fig. S11). Hence, we performed a modified system identification procedure to include the opsin dynamics in the linear dynamic system. We hypothesized that an additional order in the linear system could account for the effect of the opsin dynamics (fig. S11). We further developed our model on the basis of the ChR2 four-state photocycle model (*27*, *39*–*41*). The four-state photocycle model assumes two activation states, O1 and O2, and two deactivation states, C1 and C2. Because of the unidirectional state transition between C1 and C2 (C2 → C1), conductance in O2 activation state shows impulsive transitional dynamics under constant optical stimulation (*39*). We modeled the impulsive transitional dynamics using the axonal conductance of the open states as

$$N_{O2} = \frac{n_{O2} + a}{t_{O2} + s} \tag{3}$$

where N_{O2} and t_{O2} are the overall unit recruitment in the O2 state and a time constant for the transitional dynamics, respectively. n_{O2} and a are fitting parameters to describe the transitional and steady state of the O2 dynamics on the basis of the number of channels in each state. Then, the overall unit recruitment for O1state was defined as

$$N_{O1} = u - N_{O2} = \left(1 - \frac{n_{O2}s + a}{t_{O2} + s}\right)u \tag{4}$$

Because O1 and O2 states are known to have different conductance levels (*42*), effective unit recruitment by channels in O1 and O2 states u_{O12} was described as

$$u_{O12} = C_{O1}N_{O1} + C_{O2}N_{O2} = \frac{C_{O1}t_{O2} + (C_{O1} + (C_{O2} - C_{O1})n_{O2})s + (C_{O2} - C_{O1})a}{t_{O2} + s}u \tag{5}$$

where N_{O1} and C_{O2} are the axonal conductance for each O1 and O2 states.

In accordance with our modeling, this additional order coupled to the muscle dynamics forming a third-order system was found to closely replicate the dynamics observed experimentally ($R^2 = 0.9621$; Fig. 3H and fig. S11), with similar performance to the second-order model with non-invertible opsin dynamics ($R^2 = 0.9635$; Fig. 3G). The rest of the animals also depicted similar performance ($R^2 = 0.9292$; $n = 3$; fig. S11). A higher-order model (fourth order) showed similar performance to the third-order model (fig. S11). Together, considering the recruitment static nonlinearity (Eq. 1), muscle-tendon dynamics (Eq. 2), and opsin dynamics (Eq. 5), the resulting second-order force FES dynamics and the resulting third-order force FOS dynamics were described as

$$F_{FES} = f_R F_{MT} u \tag{6}$$

$$F_{FOS} = f_R \left[\frac{C_{O1} t_{O2} + (C_{O1} + (C_{O2} - C_{O1}) n_{O2}) s + (C_{O2} - C_{O1}) a}{t_{O2} + s} \right] F_{MT} u \tag{7}$$

High-fidelity closed-loop optogenetic muscle control

On the basis of the biophysical model, we then designed a controller to evaluate the force controllability of muscles under FOS. We hypothesized that a controller with knowledge of FOS-stimulated muscle dynamics would outperform one with only feedback. To test this, we built a model-based controller with the entire FOS and FES dynamics as a feedforward element plus feedback (MB) and one with only feedback (FB) (Fig. 4A). The feedback controller comprised a proportional-integral (PI) controller with gains adjusted at the beginning of each experiment for each animal. The feedforward controller comprised the inverted third-order muscle model of FOS and second-order FES models (inverse of Eqs. 6 and 7), plus the same PI controller. To investigate the differences between stimulation modalities, both controllers were tested using FOS and FES. The closed-loop system compares the error between a reference force trajectory and the measured force from the muscle-tendon unit and modulates the pulse width of the stimulation signal on the basis of the controller architecture (FB or MB) in real time at 2 kHz (Fig. 4A). See Materials and Methods for the detailed procedure.

We first performed closed-loop control of muscle force following square waveforms, which represent signals where steady-state force needs to be achieved, as is required in tasks like grasping and standing (Fig. 4D). Under square trajectories, we observed significantly less error when using the model-based controller under FOS (MB: 13.8%, FB: 33.2%; Fig. 4E). Under FES, the error was not different between model-based and feedback-only control (MB: 34.9%, FB: 31.4%; Fig. 4E). We then performed closed-loop control following sinusoidal force trajectories (Fig. 4B) to emulate the signal waveforms used in tasks like walking and running. Analysis of control performance revealed significantly less error using the model-based controller compared with the feedback-only controller under FOS (MB: 13.8%, FB: 33.5%; Fig. 4C). This was not the case for FES (MB: 24.7%, FB: 36.7%; Fig. 4C). Feedforward and feedback control signals for both FOS and FES contributed to the performance of the controller, as indicated by their positive value (fig. S12), underscoring the relevance of including a feedforward policy. We confirmed the ability of the model to cancel a portion of the dynamics of FOS-stimulated muscle and the applicability of the model for real-time control purposes.

We then compared the controllability between FOS and FES. For square waveforms (Fig. 4D), model-based FOS performed with significantly less error than model-based FES (FOS-MB: 13.8%, FES-MB: 34.9%; Fig. 4E) and feedback-only FES (FOS-MB: 13.8%, FES-FB: 31.4%; Fig. 4E). For sinusoidal waveforms (Fig. 4B), model-based FOS also showed significantly less error compared with model-based FES (FOS-MB: 13.8%, FES-MB: 24.7%; Fig. 4C) and feedback-only FES (FOS-MB: 13.8%, FES-FB: 36.7%; Fig. 4C). These results indicate higher controllability of FOS compared with FES given the optimal control policy for each stimulation modality.

We then evaluated control performance using rise time, settling time, and overshoot metrics. We observed significantly reduced settling times under model-based FOS compared with model-based and feedback-only FES (Fig. 4F and table S5). For rise time, significant differences were observed between model-based FOS and model-based FES control; however, no significant differences were found between model-based FOS and feedback-only FES (Fig. 4F and table S5). Feedback-only FES control showed lower rise times compared with model-based FES (Fig. 4F and table S5). For overshoot, no significant differences were observed between FOS and FES or between control modalities of FOS and FES (Fig. 4F and table S5). This suggests that the model-based controller has a predominant effect on settling time to achieve steady-state force.

Fatigue-resistant optogenetic muscle control

We further probed controller performance during an extended stimulation protocol to evaluate fatigue resistance using the model-based controller. FOS showed reduced error across the whole stimulation protocol of 62 min (Fig. 5A). At approximately minute 10, FES had a control error above 50%; at minute 11.5, the error was close to 75%; and at minute 14, the error reached up to 90%. FES was unable to modulate force at approximately 15 min (Fig. 5, A and C); hence, stimulation was stopped at 30 min after no sign of response. Unexpectedly, FOS was able to modulate force up until the end of the experiment (62 min), with errors below 50% for the whole duration (Fig. 5, A and C). The control error at 6, 15, and 30 min for FOS was 8.99, 16.23, and 42.39%, respectively, compared with 29.73, 86.86, and 82.76% for FES (Fig. 5B). At 6, 15, and 30 min, FOS had a fatigue index of 0.95, 0.99, and 0.33, respectively, compared with FES' 0.64, 0.62, and 0.75. At 6, 15, and 30 min, FOS showed increased fatigue resistance compared with FES (148, 1600, and 444%, respectively). On the basis of the reference trajectory frequency (0.6 Hz) mimicking a walking gait at 0.125 m/s (*43*), we estimated that this animal would have performed 2227 cycles walking approximately 465 m.

Periodic behavior was observed during extended closed-loop control. This periodicity can be explained by two mechanisms. The first is related to a potentiated state (*44*), characterized by increases in EMG and torque (*45*), and depends on the contractile history (*44*). This mechanism has been linked to phosphorylation of myosin light chains (*46*) and increases in α-motorneuron excitability (*44*, *47*). This was observed in both FOS and FES (fig. S13). A three-phase mechanism previously described by our group (*25*) may underlie the intermittent 2-min decrease in control performance that we found for FOS (fig. S13). Despite this, the controller was able to maintain up to 50% of force during the whole stimulation period.

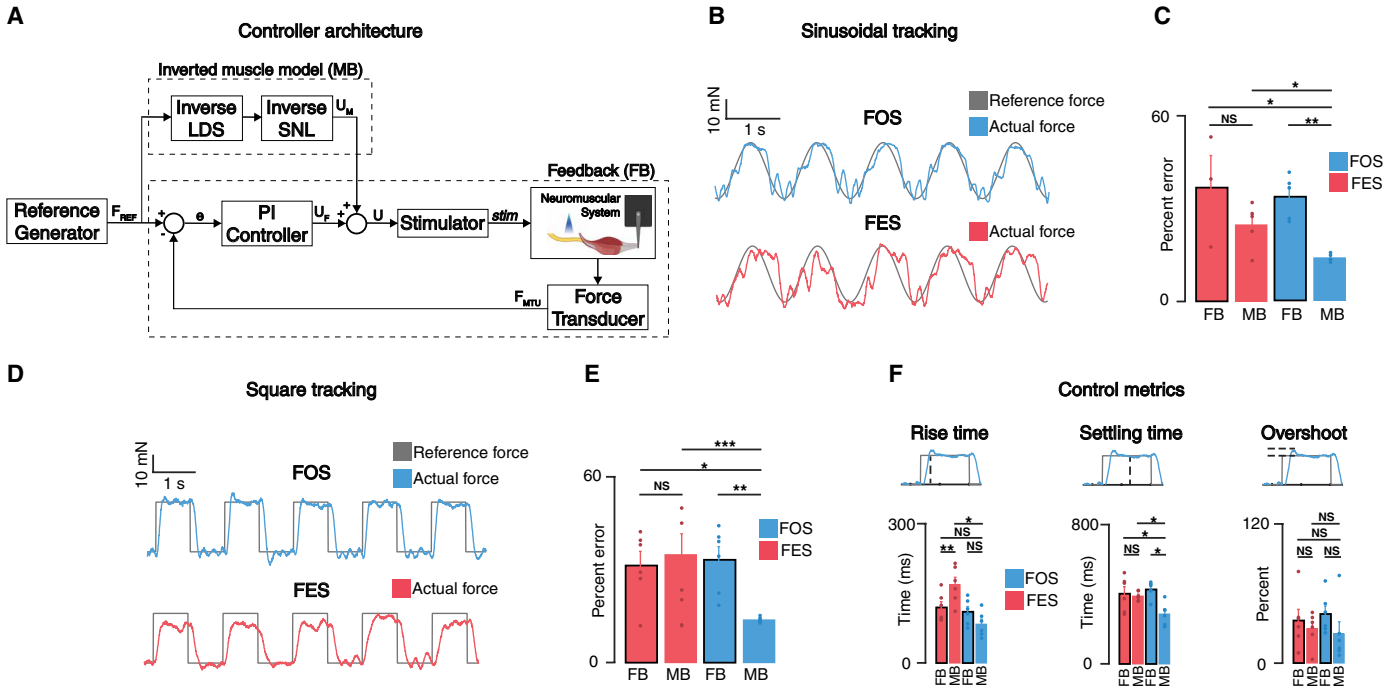

Fig. 4. Closed-loop optogenetic muscle force control. (**A**) Controller architecture detailing MB feedforward loop comprising the inverted muscle model and FB loop comprising the PI controller. F_{REF} is the reference force, e is the error, U_M is the control signal of the inverted muscle model (feedforward), U_F is the control signal of the PI controller (feedback), U is the combined signal of feedforward and feedback, stim is the command sent to the stimulator based on the control signal, and F_{MTU} is the force signal recorded at the muscle-tendon unit. (**B**) Representative force sinusoidal tracking under FOS (top) and FES (bottom). (**C**) Percent errors for MB architecture and FB architecture for FOS and FES for sinusoidal tracking ($n = 6$, FOS-MB: 687, FES-MB: 353, FOS-FB: 252, FES-FB: 212 cycles); FOS-FB versus FOS-MB $^{**}P = 0.0059$; FES-FB versus FES-MB $P = 0.2162$; FOS-MB versus FES-MB $^{*}P = 0.04$; FOS-MB versus FES-FB $^{*}P = 0.0233$. (**D**) Representative force square tracking under FOS (top) and FES (bottom). (**E**) Percent error for MB architecture and FB architecture for FOS and FES for square tracking ($n = 7$, FOS-MB: 1153, FES-MB: 590, FOS-FB: 553, FES-FB: 616 cycles); FOS-FB versus FOS-MB $^{**}P = 0.0069$; FES-FB versus FES-MB $P = 0.5782$; FOS-MB versus FES-MB $^{***}P < 0.005$; FOS-MB versus FES-FB $^{*}P = 0.0123$. (**F**) Rise time, settling time, and overshoot metrics comparison between FOS and FES and between control strategies ($n = 7$); for statistical analysis details, see table S5. Closed-loop control error is the root mean square error between reference and actual force signals. $^{**}P < 0.01$; $^{*}P < 0.05$; NS, not significant. Paired two-tailed t test at significance level ($\alpha = 0.05$). Error bars represent SEM.

This periodicity was also found in a second animal that underwent a stimulation protocol of 72 min (fig. S14).

DISCUSSION

Despite the successful demonstrations of FES motor prostheses, application of this technology is still unsuitable for chronic use in daily life, mainly because of the unnatural recruitment order of motor units that leads to muscle fatigue and poor control. Here, we established a framework to elucidate the force modulation characteristic of FOS, a technology capable of orderly recruitment of motor units. We also provided modulation strategies tailored to FOS considering its spatial and temporal dynamics, developed a neuromuscular model for optogenetic motor prostheses, and demonstrated closed-loop FOS control of muscle force with high-fidelity for extended durations.

Dexterous grasping, object manipulation, and complex tasks like playing the piano require exquisite neural control of muscles. A principle of neuromuscular organization that is thought to allow such control is the size principle (*20*, *21*) or orderly recruitment of motor units. It has been shown that axon conduction latencies under FOS closely replicate this principle (*19*). On the basis of this finding, we hypothesized that force modulation using FOS would be more physiological than FES. We provide data to support this hypothesis. FOS achieves proportional, graded, and more-linear force modulation compared with FES. Given the recruitment mechanism of FES, large-diameter axons are activated at lower thresholds, limiting the modulation efficiency. Because of the uniform presence of photosensitive channels in small and large axons leading to membrane potential thresholds similar to physiological ones, FOS yields a modulation characteristic where force production is proportional to the given stimulation, similar to the physiological mechanism observed when muscles are naturally activated. This modulation characteristic adds evidence to support the hypothesis that FOS achieves orderly recruitment of motor units, although studies where isolated motor axons are optically stimulated might help determine the specific recruitment order (*48*). Higher force magnitude was observed under FOS compared with FES, revealing greater access to motor units using an extraneural stimulation modality. Given the fixed firing rate of individual motor units (constant stimulation frequency), the force differences can be attributed to the recruitment of additional motor units. The inaccessibility of FES to a population of motor units could be explained by the structural barrier between the electrode contacts and fibers in deeper fascicles because of the transversal topography of fibers within a nerve when an extraneural electrical interface is used (*49*). Moreover, because of the preferential excitability of large fibers during

FES, additional fibers that could be recruited limit the total output muscle force (*50*, *51*). An analysis of opsin expression in the sciatic nerves of ChR2 transgenic mice revealed no correlation with axon diameter (*19*); this suggests that our results could extend to muscles with different fiber compositions than the one studied here. Overall, the uniform expression of photosensitive channels and its optical activation confer muscles with a recruitment characteristic suited for physiological force modulation using artificial stimulation.

Given optogenetic transduction, we described spatial considerations for optical nerve stimulation. We reported a proximodistal behavior when using FOS, which elicited different force responses depending on the stimulation site. When stimulation was performed closer to the muscle, responses exhibited sustained force generation and higher force resolution between stimulation levels compared with proximal stimulation. This suggested that optical stimulation closer to the muscle is preferred over proximal stimulation. We hypothesized that this is because of a variation in expression of ChR2 levels along the nerve. A spatial behavior has been reported for ChR2-transfected primary afferent neurons where excitability differences were observed between distal and proximal sections of the axons (*52*), and in simulations, it has been suggested that optogenetic stimulation of different parts of a pyramidal neuron will evoke different spiking patterns (*53*). However, our results indicate a similar ChR2 expression profile between proximal and distal nerve regions. A potential explanation is the anatomical differences in axonal distribution at proximal and distal nerve locations, where proximal locations contain fibers that innervate other muscles and, hence, light penetration to fibers of interest becomes harder to achieve compared with distal regions. Beyond recruitment, another mechanism to modulate force is rate coding. We described a similar modulation profile between FOS and FES up to 40 Hz, whereas after 40 Hz, force under FOS started to decrease, likely because of a desensitization of excitatory opsin ChR2 (*27*, *28*). Notably, force magnitudes attained under FOS were higher up to 40 to 50 Hz, and at higher frequencies where ChR2 starts to desensitize, there were no significant differences compared to FES.

Neuromuscular models have contributed to the understanding of motor control and the development of FES neuroprostheses. We conceived a neuromuscular model that closely replicated muscle dynamics under FOS. Our model considers muscle recruitment, opsin dynamics, and muscle-tendon dynamics to build a biophysical model that recapitulates optogenetic-mediated muscle dynamics. The selected order of components is based on a Hammerstein structure and an associated identification procedure to ensure that the model parameters can be estimated independently of the nonlinearity; however, it is plausible to have a model where the opsin dynamics appear first, followed by the recruitment and muscle dynamics. Having established a paradigm to model force dynamics, we assessed the elemental difference between FOS and FES. As expected, this difference corresponds to transitional dynamics between the photocycle kinetics of the opsin, which contributes to the decay observed in the FOS force profiles. Although the model was described under isometric conditions, the extension of the model to dynamic conditions, such as limb control applications, was chronicled in our modeling. Nevertheless, it is necessary to assess the closed-loop control performance observed in our study to determine the extent to which our modeling can be applied to dynamic settings. Because of the cascade modeling architecture used here, each block of our model can be easily linked to particular biophysical dynamics for further probing and improvement of the model and for extending this model to different expression levels on the basis of gene delivery method, opsins, optical delivery methods such as transdermal stimulation, or other nervous tissues. Moreover, our model can be readily used in other neuromuscular architectures and could be advantageous to the development of neuromusculoskeletal models to more accurately represent physiological muscle dynamics.

Last, we provided a demonstration of closed-loop force control using FOS. We hypothesized that knowledge of the optically stimulated muscle dynamics would enable the development of a controller that confers greater muscle controllability and that all things equal, muscle control would be superior under FOS compared with FES. Our study provides data to support these hypotheses. Our model is suited for real-time control applications, and when the model-based controller was compared with a model-less controller under FOS, it exhibited significantly less error under square and sinusoidal trajectories.

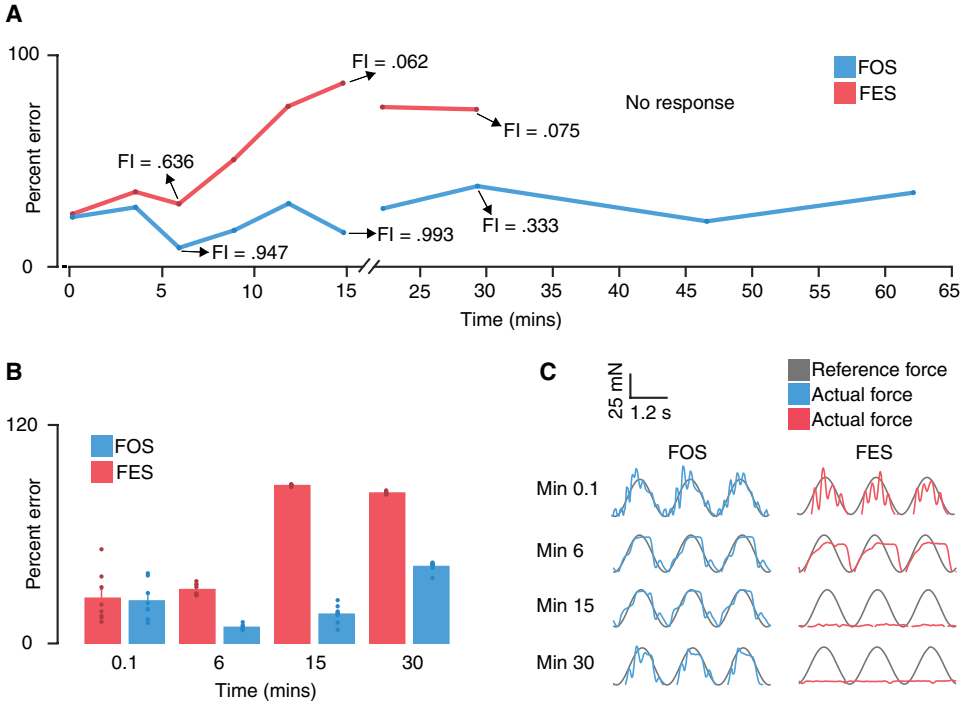

Fig. 5. Fatigue-resistant optogenetic muscle control. (**A**) Representative trial of closed-loop percent error over time between FOS and FES. (**B**) Closed-loop percent error for FOS and FES at 0.1, 6, 15, and 30 min. (**C**) Representative closed-loop force tracking for FOS (left) and FES (right) for 0.1, 6, 15, and 30 min. FI, fatigue index. Closed-loop control error is the root mean square error between reference and actual force signals. Error bars represent SEM.

We also demonstrated high-fidelity force control under FOS, as shown by significantly less error when compared with FES for both square and sinusoidal trajectories. Although a number of controllers can be designed on the basis of other model architectures and the detailed contribution of each of the feedforward terms requires further investigation, our results stress the benefit of having a feedforward control policy based on a biophysical model that best describes muscle dynamics under each stimulation modality. Our model-based FOS controller seemed to have a substantial effect on the settling time, suggesting that the force decay opsin dynamics can be advantageous when included in the controller. Although the frequencies of the reference trajectories used here are slower than typical walking and running frequencies in both rodents and humans, we showed closed-loop control and maintenance of steady-state force, which are required for sustained control in a number of tasks (*1*). Previously, our group described position control of the ankle in rodents; together, FOS enables greater position and force controllability, where, for a number of demanding tasks, both are usually used in combination for isometric and isotonic loads (*25*, *54*, *55*). We further demonstrated that FOS enables fatigue-resistant muscle control. We subjected our controller to a 62-min protocol and found that FES fatigues around 15 min, showing similar signs of early fatigue compared to previous studies despite the stimulation target (*56*) or stimulation protocol (*30*, *57*–*59*). In contrast, FOS was able to maintain muscle control until the end of the protocol with less than 50% error. When FOS was delivered to the muscle, the fatigue behavior between FOS and FES was similar (*60*), suggesting that the delivery of FOS to the nerve and opsin expression limited to neural tissue might be preferred. We also provided additional data of the fatigue dynamics of FOS. We found a time-dependent potentiated state that elicited muscle overactivity; this was observed under FOS and FES control. We also observed phasic control properties in agreement with the time-variant model previously proposed by our group (*25*). Accurate fatigue-resistant closed-loop muscle control might be advantageous beyond motion restoration. Neuroprosthetic architectures, such as the agonist-antagonist myoneural interface (*61*) or cutaneous mechanoneural interface (*62*), rely on accurate closed-loop artificial stimulation to convey proprioceptive and cutaneous feedback. Moreover, optogenetic-based biohybrid actuators (*63*) could benefit from the methodologies, modulation strategies, and model-based control policies described here.

The advancements in FOS have paved the way for the development of novel therapeutics. Clinical trials in phase 1/2 are now demonstrating the use of multicharacteristic opsins: ChR2, ChrimsonR, and ChronosFP, delivered through adenosine-associated viruses (AAVs), to restore vision in retinitis pigmentosa and Stargardt disease (*64*). However, to realize the first optogenetic motor prosthesis and extend the application of optogenetic technology beyond the eye into the peripheral nervous system (PNS), several challenges must be addressed. First, real-time and accurate stimulation and sensing of the PNS are challenging. Light delivery to the PNS is complicated because of its considerable movement with the body, tissue penetration depth, and the energy expenditure of optogenetics (*65*, *66*). An optimal light delivery system will allow for freedom of movement, deliver sufficient energy (1 to 5 mW mm^{-2}), and cause minimal heating (*65*, *67*, *68*). Tissue penetration depth can be extended by using red-shifted opsins to target deeper neural structures (*68*). Challenges related to displacement of neural tissue targets for light delivery can be minimized by using conformable and affixed implantable systems (*69*, *70*). In regard to sensing, direct muscle-tendon force sensing as presented here might be challenging; although there exist some implantable strategies (*71*), muscle length sensing using magnetomicrometry (*72*) or noninvasive muscle-tendon force estimation (*73*) might be more practical. Second, opsin delivery to the PNS remains challenging. Although germline modification as shown here is not viable for translation, opsin gene delivery through viral transduction is the most plausible in humans (*65*, *67*, *68*, *74*). AAVs are the preferred viral vectors for gene delivery because of their extensive use in humans, relatively low immunogenicity, and nonpathogenic nature (*65*, *67*, *68*, *74*); however, further optimization for specific therapies to overcome the challenges of poor transduction efficiency and preexisting immune response to certain AAV serotypes is required (*68*, *75*). Third, sustaining long-term opsin expression in neuronal populations is difficult. Opsins have been known to cause an immune response, especially in the periphery because of greater immune surveillance, which can substantially reduce opsin levels over time (*76*). Immunosuppressive treatment with tacrolimus and the engineering of new opsins that elicit smaller immune responses have been proposed as solutions (*74*, *76*). In addition, further work is required to extend the opsin toolkit to enable multidimensional optogenetic control beyond two wavelengths (*68*, *77*). These challenges require extensive clinical and scientific investment and must be overcome to realize optogenetic translation.

Together, our results provide a framework and outline key principles for the development of optogenetically modulated muscle actuation. Such actuation has the potential to become a viable alternative to electrical stimulation in neural prostheses for motion restoration and pave the way for high-performance biohybrid systems.

MATERIALS AND METHODS

Study design

The main objective of the study was to design a control framework that enabled accurate and fatigue-resistant control of skeletal muscle using artificial stimulation. Experiments in this study were designed to characterize the muscle dynamics of FOS, develop a biophysical muscle model, and perform closed-loop control of muscle force. Experiments were conducted on Thy1-ChR2-YFP mice (the Jackson Laboratory, strain #007612). These animals express light-sensitive ion channel ChR2 fused to yellow fluorescent protein under control of mouse thymus cell antigen (*Thy1*) promoter. Animals were 12 weeks old and weighed 18.2 ± 1.3 g at the time of the experiment. All experimental procedures were approved by the Committee on Animal Care at the Massachusetts Institute of Technology. Two different groups were used, the first for muscle characterization and system identification experiments ($n = 8$); replicates are described in the "Stimulation protocols" section of the Materials and Methods and in the "Modeling" section of the Supplementary Methods. The second group was used for closed-loop experiments ($n = 7$); replicates are described in the legend of Fig. 4 and in the "Extended closed-loop control experiments" section of the Materials and Methods. There were no inclusion or exclusion criteria.

Muscle force recordings

To precisely measure muscle force in small animal models, a muscle characterization apparatus was developed comprising a recording

and stimulation platform. The platform includes a dual-mode lever muscle tensioning system (Aurora Scientific) equipped with a force transducer capable of measuring forces within 0 to 10 N with a resolution of 1.0 mN. The system operates at a sampling rate of 2 kHz. The platform allows for adjustment in three degrees of freedom, which is critical to ensure proper alignment of the muscle-tendon unit with the force transducer, thereby guaranteeing that all the force is measured in the contractile direction. The stimulation platform comprises a lever with adjustments in three degrees of freedom for accurate positioning of the light-emitting diode and hook electrode along the peripheral nerve. The apparatus also has a compartment where a heat pad can be placed to control the body temperature of the animal. The platform was fabricated via three-dimensional (3D) printing using a Connex 500 machine (Stratasys) and vero black plus material, a high-strength ultraviolet-cured polymer for high-resolution prototypes. Figure S1 shows that force pulses under FOS and FES from a muscle-tendon unit displayed consistent baseline levels between pulses, indicating that the measuring setup was exclusively capturing the muscle contraction force. The baseline force is not zero because an initial tension is necessary to maintain the muscle at a constant length and to minimize slack of the string between the tendon and the force transducer. Raw force signals were low-pass–filtered (10th-order filter) using a pass band frequency at 50 Hz. Signals were zeroed by subtracting the initial force offset and then time-segmented on the basis of a digital trigger from the optical or electrical stimulator. Peak force is the maximum value for each force profile. Steady-state force is the average of a 100-ms window, starting 100 ms before the end of the 2.0-s stimulus duration.

Stimulation protocols

We performed a suite of stimulation protocols aimed at characterizing the muscle spatiotemporal dynamics of FOS. For comparison, FES was delivered at the contralateral leg of the same animal. Stimulation modality at start was randomly determined. Modulation of the amplitude or pulse width of the stimulation signal recruits additional motor units, both under FES (*1*) and FOS (*28*). Here, amplitude modulation was used to characterize the spatial behavior (fig. S3) and to determine the muscle force range to allow for a fair comparison of recruitment curves between FOS and FES. Pulse width modulation was used to elucidate the recruitment characteristic with knowledge of the muscle force range from the amplitude modulation experiments. Frequency was set to 60 Hz to ensure tetanic contraction, because frequencies below 60 Hz present ripple, which could impede accurate force control (*19*, *28*), and to ensure that absolute force magnitudes between FOS and FES were not significantly different. For rate coding characterization, frequency modulation was used. At the beginning of each trial, using constant frequency and pulse width, stimulation was conducted at different amplitudes while observing the force profiles to determine the minimum and maximum stimulation amplitude for each animal. Frequency was set to 60 Hz to ensure tetanic contraction. Pulse width was set to 5% of stimulation frequency (0.83 ms) to minimize heating according to safety guidelines previously established (*25*). On the basis of the minimum and maximum values, amplitude sweeps were performed at the aforementioned frequency and pulse width. Amplitude sweeps were used to characterize the spatial behavior. Then, we performed pulse width sweeps. Stimulation amplitude was set on the basis of one that generated close to 33% of maximum peak force in the amplitude sweep experiment. We reasoned that because the amplitude sweep was performed at a pulse width of 5% of stimulation frequency (0.83 ms), a pulse width sweep from 0 to 15% of stimulation frequency (0 to 2.5 ms) would modulate the full range of force at that particular amplitude. Frequency was set to 60 Hz. We then performed frequency sweeps. Stimulation amplitude was set on the basis of one that generated close to 66% of the maximum peak force in the amplitude sweep experiment. We reasoned that because the amplitude sweep was performed at 60 Hz, a 0- to 100-Hz range would modulate the full range of force. Pulse width was set to 0.83 ms (5% of 60-Hz stimulation frequency). Stimulation was carried out from maximum to minimum. All stimulation sweeps were performed two times under each stimulation modality for each animal.

Closed-loop control system design

The closed-loop control system was implemented in LabVIEW 2019 (National Instruments), running real time in an NI myRIO microcontroller. The feedback loop comprised a PI controller that computed an error on the basis of the reference signal and the signal from the force transducer recorded at 2 kHz. The controller outputs a digital signal either to the optical or electrical stimulator of the stimulation pulse width. For the feedforward loop, the biophysical muscle model was converted into discrete time and computed in real time at 2 kHz on the basis of the reference signal. The output signal of the feedforward component was added to the feedback signal and sent to the electrical or optical stimulator.

Closed-loop control experiments

Before closed-loop procedures, an amplitude sweep was carried out to determine the muscle force range for a particular animal. On this basis, the stimulation amplitude was set to one that generated around 50% of the maximum muscle force. The amplitude of the reference waveform, either square or sinusoidal, was set to be 20 to 30% of the maximum muscle force. Frequency of the reference signals was between 0.6 and 0.8 Hz. First, the PI gains were adjusted using feedback only. Once the optimal PI gains were determined for each animal on the basis of the rise time, settling time, and overshoot of the control signal under square waveforms, closed-loop experiments were performed for approximately 60 s without modifying the gains for square waveform experiments. Then, the model (feedforward) was incorporated with the same PI controller, and closed-loop experiments were carried out under square waveforms. After this, closed-loop experiments were performed under sinusoidal waveforms, first with feedback-only control and then with the model-based control. Similarly, the same gains were maintained. As in the stimulation protocols, FOS was performed on one leg, whereas FES was performed on the contralateral one. Closed-loop control error was computed as the root square mean error between the reference and the actual force signal of the steady-state portion under square waveforms and the positive cycle under sinusoidal waveforms.

Extended closed-loop control experiments

Extended closed-loop control procedures were carried out after 15 min of closed-loop procedures from the previous section to allow for resting the muscle. Using the same model-based controller as in the previous section, closed loop was performed for 62 min. Because the objective of this experiment was to show closed-loop

control for more than 1 hour, we decided to stop the stimulation just after 60 min. The amplitude of the reference sinusoidal waveform was set to be 20 to 30% of the maximum muscle force at a 0.6-Hz frequency. For both FOS and FES, there were approximately 10 s of pause every 10 min to allow data in the LabVIEW software to be saved. Extended closed-loop control experiments were only performed in two animals (Fig. 5 and figs. S13 and S14). Fatigue index was computed as the mean force at a particular time point divided by the initial force.

Statistics

All data were exported and processed in MATLAB (R2022a, MathWorks, Natick, MA, USA). All data are reported as mean or mean ± SEM, unless otherwise reported. Paired two-tailed t test at significance level ($\alpha = 0.05$) was used for all comparisons between FOS and FES where P values are displayed, unless otherwise reported. Normal distribution was validated using the Shapiro-Wilk test.

Supplementary Materials

This PDF file includes:
Supplementary Methods
Figs. S1 to S17
Tables S1 to S5

Other Supplementary Material for this manuscript includes the following:
MDAR Reproducibility Checklist

REFERENCES AND NOTES

1. W. K. Durfee, K. E. Maclean, Methods for estimating isometric recruitment curves of electrically stimulated muscle. *IEEE Trans. Biomed. Eng.* **36**, 654–666 (1989).
2. H. J. Chizeck, P. E. Crago, L. S. Kofman, Robust closed-loop control of isometric muscle force using pulsewidth modulation. *IEEE Trans. Biomed. Eng.* **35**, 510–517 (1988).
3. L. A. Bernotas, P. E. Crago, H. J. Chizeck, A discrete-time model of electrically stimulated muscle. *IEEE Trans. Biomed. Eng.* **33**, 829–838 (1986).
4. P. E. Crago, P. H. Peckham, G. B. Thrope, Modulation of muscle force by recruitment during intramuscular stimulation. *IEEE Trans. Biomed. Eng.* **27**, 679–684 (1980).
5. A. J. Bergquist, J. M. Clair, D. F. Collins, Motor unit recruitment when neuromuscular electrical stimulation is applied over a nerve trunk compared with a muscle belly: Triceps surae. *J. Appl. Physiol.* **110**, 627–637 (2011).
6. W. Trojaborg, Motor nerve conduction velocities in normal subjects with particular reference to the conduction in proximal and distal segments of median and ulnar nerve. *Electroencephalogr. Clin. Neurophysiol.* **17**, 314–321 (1964).
7. T. Ito, E. Z. Murano, H. Gomi, Fast force-generation dynamics of human articulatory muscles. *J. Appl. Physiol.* **96**, 2318–2324 (2004).
8. J.-K. Lim, M.-H. Nam, G. Khang, Model of activation dynamics for an FES-induced muscle fatigue, in *Proceedings of the 22nd Annual International Conference of the IEEE Engineering in Medicine and Biology Society* (IEEE, 2000), pp. 2251–2253.
9. S. J. Dorgan, M. J. O'Malley, A nonlinear mathematical model of electrically stimulated skeletal muscle. *IEEE Trans. Rehabil. Eng.* **5**, 179–194 (1997).
10. Y. Giat, J. Mizrahi, M. Levy, A musculotendon model of the fatigue profiles of paralyzed quadriceps muscle under FES. *IEEE Trans. Biomed. Eng.* **40**, 664–674 (1993).
11. R. Riener, J. Quinternt, G. Schmidt, Biomechanical model of the human knee evaluated by neuromuscular stimulation. *J. Biomech.* **29**, 1157–1167 (1996).
12. C. Ethier, E. R. Oby, M. J. Bauman, L. E. Miller, Restoration of grasp following paralysis through brain-controlled stimulation of muscles. *Nature* **485**, 368–371 (2012).
13. W. D. Memberg, K. H. Polasek, R. L. Hart, A. M. Bryden, K. L. Kilgore, G. A. Nemunaitis, H. A. Hoyen, M. W. Keith, R. F. Kirsch, Implanted neuroprosthesis for restoring arm and hand function in people with high level tetraplegia. *Arch. Phys. Med. Rehabil.* **95**, 1201–1211.e1 (2014).
14. A. B. Ajiboye, F. R. Willett, D. R. Young, W. D. Memberg, B. A. Murphy, J. P. Miller, B. L. Walter, J. A. Sweet, H. A. Hoyen, M. W. Keith, P. H. Peckham, J. D. Simeral, J. P. Donoghue, L. R. Hochberg, R. F. Kirsch, Restoration of reaching and grasping movements through brain-controlled muscle stimulation in a person with tetraplegia: A proof-of-concept demonstration. *Lancet* **389**, 1821–1830 (2017).
15. A. Sturma, O. Schuhfried, T. Hasenoehrl, C. Ambrozy, S. Salminger, L. A. Hruby, J. A. Mayer, K. Götz-Neumann, R. Crevenna, M. M. Pinter, O. C. Aszmann, The long-term effects of an implantable drop foot stimulator on gait in hemiparetic patients. *PLOS ONE* **14**, e0214991 (2019).
16. J. H. Burridge, P. N. Taylor, S. A. Hagan, D. E. Wood, I. D. Swain, The effects of common peroneal stimulation on the effort and speed of walking: A randomized controlled trial with chronic hemiplegic patients. *Clin. Rehabil.* **11**, 201–210 (1997).
17. F. Berenpas, V. Weerdesteyn, A. C. Geurts, N. Van Alfen, Long-term use of implanted peroneal functional electrical stimulation for stroke-affected gait: The effects on muscle and motor nerve. *J. Neuroeng. Rehabil.* **16**, 86 (2019).
18. R. P. Onders, M. J. Elmo, S. Khansarinia, B. Bowman, J. Yee, J. Road, B. Bass, B. Dunkin, P. E. Ingvarsson, M. Oddsdóttir, Complete worldwide operative experience in laparoscopic diaphragm pacing: Results and differences in spinal cord injured patients and amyotrophic lateral sclerosis patients. *Surg. Endosc.* **23**, 1433–1440 (2009).
19. M. E. Llewellyn, K. R. Thompson, K. Deisseroth, S. L. Delp, Orderly recruitment of motor units under optical control in vivo. *Nat. Med.* **16**, 1161–1165 (2010).
20. E. Henneman, Relation between size of neurons and their susceptibility to discharge. *Science* **126**, 1345–1347 (1957).
21. E. Henneman, G. Somjen, D. Carpenter, Functional significance of cell size in spinal motoneurons. *J. Neurophysiol.* **28**, 560–580 (1965).
22. G. F. Wilhere, P. E. Crago, H. J. Chizeck, Design and evaluation of a digital closed-loop controller for the regulation of muscle force by recruitment modulation. *IEEE Trans. Biomed. Eng.* **32**, 668–676 (1985).
23. V. K. Mushahwar, P. L. Jacobs, R. A. Normann, R. J. Triolo, N. Kleitman, New functional electrical stimulation approaches to standing and walking. *J. Neural Eng.* **4**, 181–197 (2007).
24. D. Popovic, L. L. Baker, G. E. Loeb, Recruitment and comfort of BION implanted electrical stimulation: Implications for FES applications. *IEEE Trans. Neural Syst. Rehabil. Eng.* **15**, 577–586 (2007).
25. S. S. Srinivasan, B. E. Maimon, M. Diaz, H. Song, H. M. Herr, Closed-loop functional optogenetic stimulation. *Nat. Commun.* **9**, 5303 (2018).
26. E. S. Boyden, F. Zhang, E. Bamberg, G. Nagel, K. Deisseroth, Millisecond-timescale, genetically targeted optical control of neural activity. *Nat. Neurosci.* **8**, 1263–1268 (2005).
27. G. Nagel, T. Szellas, W. Huhn, S. Kateriya, N. Adeishvili, P. Berthold, D. Ollig, P. Hegemann, E. Bamberg, Channelrhodopsin-2, a directly light-gated cation-selective membrane channel. *Proc. Natl. Acad. Sci. U.S.A.* **100**, 13940–13945 (2003).
28. C. Towne, K. L. Montgomery, S. M. Iyer, K. Deisseroth, S. L. Delp, Optogenetic control of targeted peripheral axons in freely moving animals. *PLOS ONE* **8**, e72691 (2013).
29. A. J. Fuglevand, D. A. Winter, A. E. Patla, Models of recruitment and rate coding organization in motor-unit pools. *J. Neurophysiol.* **70**, 2470–2488 (1993).
30. Z. P. Fang, J. T. Mortimer, A method to effect physiological recruitment order in electrically activated muscle. *IEEE Trans. Biomed. Eng.* **38**, 175–179 (1991).
31. K. Emancipator, M. H. Kroll, A quantitative measure of nonlinearity. *Clin. Chem.* **39**, 766–772 (1993).
32. J. J. Williams, A. M. Watson, A. L. Vazquez, A. B. Schwartz, Viral-mediated optogenetic stimulation of peripheral motor nerves in non-human primates. *Front. Genet.* **13**, 759 (2019).
33. P. Z. Marmarelis, K. I. Naka, White-noise analysis of a neuron chain: An application of the Wiener theory. *Science* **175**, 1276–1278 (1972).
34. B. N. Segal, J. S. Outerbridge, Vestibular (semicircular canal) primary neurons in bullfrog: Nonlinearity of individual and population response to rotation. *J. Neurophysiol.* **47**, 545–562 (1982).
35. F. Le, I. Markovsky, C. Freeman, E. Rogers, Identification of electrically stimulated muscle after stroke, in *2009 European Control Conference (ECC)* (IEEE, 2014), pp. 1676–1581.
36. J. D. Enderle, E. J. Engelken, R. N. Stilles, A comparison of static and dynamic characteristics between rectus eye muscle and linear muscle model predictions. *IEEE Trans. Biomed. Eng.* **38**, 1235–1245 (1991).
37. S. Zhao, J. T. Ting, H. E. Atallah, L. Qiu, J. Tan, B. Gloss, G. J. Augustine, K. Deisseroth, M. Luo, A. M. Graybiel, G. Feng, Cell type-specific channelrhodopsin-2 transgenic mice for optogenetic dissection of neural circuitry function. *Nat. Methods* **8**, 745–752 (2011).
38. I. W. Hunter, M. J. Korenberg, The identification of nonlinear biological systems: Wiener and hammerstein cascade models. *Biol. Cybern.* **55**, 135–144 (1986).
39. R. S. Weiss, A. Voss, W. Hemmert, Optogenetic stimulation of the cochlea—A review of mechanisms, measurements, and first models. *Network* **27**, 212–236 (2016).
40. T. J. Foutz, R. L. Arlow, C. C. McIntyre, Theoretical principles underlying optical stimulation of a channelrhodopsin-2 positive pyramidal neuron. *J. Neurophysiol.* **107**, 3235–3245 (2012).
41. N. Grossman, K. Nikolic, C. Toumazou, P. Degenaar, Modeling study of the light stimulation of a neuron cell with channelrhodopsin-2 mutants. *IEEE Trans. Biomed. Eng.* **58**, 1742–1751 (2011).
42. K. Nikolic, N. Grossman, M. S. Grubb, J. Burrone, C. Toumazou, P. Degenaar, Photocycles of channelrhodopsin-2. *Photochem. Photobiol.* **85**, 400–411 (2009).

43. C. Bellardita, O. Kiehn, Phenotypic characterization of speed-associated gait changes in mice reveals modular organization of locomotor networks. *Curr. Biol.* **25**, 1426–1436 (2015).
44. M. Hodgson, D. Docherty, D. Robbins, Post-activation potentiation. *Sports Med.* **35**, 585–595 (2005).
45. A. Erfanian, H. J. Chizeck, R. M. Hashemi, Excitation-contraction fatigue during sustained electrical stimulation of paralyzed muscle, in *Proceedings of the 18th Annual International Conference of the IEEE Engineering in Medicine and Biology Society* (IEEE, 1996), pp. 1460–1461.
46. H. L. Sweeney, B. F. Bowman, J. T. Stull, Myosin light chain phosphorylation in vertebrate striated muscle: Regulation and function. *Am. J. Physiol. Cell Physiol.* **264**, 85–95 (1993).
47. A. Van Boxtel, Differential effects of low-frequency depression, vibration-induced inhibition, and posttetanic potentiation on H-reflexes and tendon jerks in the human soleus muscle. *J. Neurophysiol.* **55**, 551–568 (1986).
48. F. E. Zajac, J. S. Faden, Relationship among recruitment order, axonal conduction velocity, and muscle-unit properties of type-identified motor units in cat plantaris muscle. *J. Neurophysiol.* **53**, 1303–1322 (1985).
49. J. Badia, A. Pascual-Font, M. Vivo, E. Udina, X. Navarro, Topographical distribution of motor fascicles in the sciatic-tibial nerve of the rat. *Muscle Nerve* **42**, 192–201 (2010).
50. M. H. Trimble, R. M. Enoka, Mechanisms underlying the training effects associated with neuromuscular electrical stimulation. *Phys. Ther.* **71**, 273–280 (1991).
51. M. Heyters, A. Carpentier, J. Duchateau, K. Hainaut, Twitch analysis as an approach to motor unit activation during electrical stimulation. *Can. J. Appl. Physiol.* **19**, 451–461 (1994).
52. Y. Zhu, B. Feng, E. S. Schwartz, G. F. Gebhart, S. A. Prescott, Novel method to assess axonal excitability using channelrhodopsin-based photoactivation. *J. Neurophysiol.* **113**, 2242–2249 (2015).
53. N. Grossman, V. Simiaki, C. Martinet, C. Toumazou, S. R. Schultz, K. Nikolic, The spatial pattern of light determines the kinetics and modulates backpropagation of optogenetic action potentials. *J. Comput. Neurosci.* **34**, 477–488 (2013).
54. P. E. Crago, J. T. Mortimer, P. H. Peckham, Closed-loop control of force during electrical stimulation of muscle. *IEEE Trans. Biomed. Eng.* **27**, 306–312 (1980).
55. J. Houk, W. Z. Rymer, Neural control of muscle length and tension, in *Handbook of Physiology, The Nervous System, Motor Control* (American Physiological Society, 1981) suppl. 2, pp. 257–323.
56. N. Wenger, E. M. Moraud, S. Raspopovic, M. Bonizzato, J. DiGiovanna, P. Musienko, M. Morari, S. Micera, G. Courtine, Closed-loop neuromodulation of spinal sensorimotor circuits controls refined locomotion after complete spinal cord injury. *Sci. Transl. Med.* **6**, 255ra133 (2014).
57. G. P. Braz, M. Russold, G. M. Davis, Functional electrical stimulation control of standing and stepping after spinal cord injury: A review of technical characteristics. *Neuromodulation* **12**, 180–190 (2009).
58. M. O. Ibitoye, N. A. Hamzaid, N. Hasnan, A. K. A. Wahab, G. M. Davis, Strategies for rapid muscle fatigue reduction during FES exercise in individuals with spinal cord injury: A systematic review. *PLOS ONE* **11**, e0149024 (2016).
59. D. McDonnall, G. A. Clark, R. A. Normann, Interleaved, multisite electrical stimulation of cat sciatic nerve produces fatigue-resistant, ripple-free motor responses. *IEEE Trans. Neural Syst. Rehabilit. Eng.* **12**, 208–215 (2004).
60. T. Bruegmann, T. Van Bremen, C. C. Vogt, T. Send, B. K. Fleischmann, P. Sasse, Optogenetic control of contractile function in skeletal muscle. *Nat. Commun.* **6**, 7153 (2015).
61. T. R. Clites, M. J. Carty, J. B. Ullauri, M. E. Carney, L. M. Mooney, J. F. Duval, S. S. Srinivasan, H. M. Herr, Proprioception from a neurally controlled lower-extremity prosthesis. *Sci. Transl. Med.* **10**, eaap8373 (2018).
62. S. S. Srinivasan, H. M. Herr, A cutaneous mechanoneural interface for neuroprosthetic feedback. *Nat. Biomed. Eng.* **6**, 731–740 (2022).
63. L. Ricotti, B. Trimmer, A. W. Feinberg, R. Raman, K. K. Parker, R. Bashir, M. Sitti, S. Martel, P. Dario, A. Menciassi, Biohybrid actuators for robotics: A review of devices actuated by living cells. *Sci. Robot.* **2**, eaaq0495 (2017).
64. D. Sakai, H. Tomita, A. Maeda, Optogenetic therapy for visual restoration. *Int. J. Mol. Sci.* **23**, 15041 (2022).
65. K. L. Montgomery, S. M. Iyer, A. J. Christensen, K. Deisseroth, S. L. Delp, Beyond the brain: Optogenetic control in the spinal cord and peripheral nervous system. *Sci. Transl. Med.* **8**, 337rv5 (2016).
66. C. L. Sanghoon Lee, Toward advanced neural interfaces for the peripheral nervous system (PNS) and their future applications. *Curr. Opin. Biomed. Eng.* **6**, 130–137 (2018).
67. J. C. Williams, T. Denison, From optogenetic technologies to neuromodulation therapies. *Sci. Transl. Med.* **5**, 177ps6 (2013).
68. A. Bansal, S. Shikha, Y. Zhang, Towards translational optogenetics. *Nat. Biomed. Eng.* **7**, 349–369 (2022).
69. E. B. Knudsen, K. Zappitelli, J. Brown, J. Reeder, K. S. Smith, M. Rostov, J. Choi, A. Rochford, N. Slager, S. K. Miura, K. Rodgers, A. Reed, Y. R. L. Israeli, S. Shiraga, K. J. Seo, C. Wolin, M. Eltaeb, A. Dasgupta, P. Chong, S. Charles, M. Jay, R. A. Silva, T. Kim, Y. Kong, A. R. Mardinly, M. Hodak, A thin-film optogenetic visual prosthesis. *bioRxiv* (2023), https://biorxiv.org/content/10.1101/2023.01.31.526482v1.
70. C. Kathe, F. Michoud, P. Schönle, A. Rowald, N. Brun, J. Ravier, I. Furfaro, V. Paggi, K. Kim, S. Soloukey, L. Asboth, T. H. Hutson, I. Jelescu, A. Philippides, N. Alwahab, J. Gandar, D. Huber, C. I. De Zeeuw, Q. Barraud, Q. Huang, S. P. Lacour, G. Courtine, Wireless closed-loop optogenetics across the entire dorsoventral spinal cord in mice. *Nat. Biotechnol.* **40**, 198–208 (2021).
71. C. M. Boutry, Y. Kaizawa, B. C. Schroeder, A. Chortos, A. Legrand, Z. Wang, J. Chang, P. Fox, Z. Bao, A stretchable and biodegradable strain and pressure sensor for orthopaedic application. *Nat. Electron.* **1**, 314–321 (2018).
72. C. R. Taylor, S. S. Srinivasan, S. H. Yeon, M. K. O. Donnell, T. J. Roberts, H. M. Herr, Magnetomicrometry. *Sci. Robot.* **6**, eabg0656 (2021).
73. J. A. Martin, S. C. E. Brandon, E. M. Keuler, J. R. Hermus, A. C. Ehlers, D. J. Segalman, M. S. Allen, D. G. Thelen, Gauging force by tapping tendons. *Nat. Commun.* **9**, 2–10 (2018).
74. L. A. Gundelach, M. A. Hüser, D. Beutner, P. Ruther, T. Bruegmann, Towards the clinical translation of optogenetic skeletal muscle stimulation. *Pflugers Arch.* **472**, 527–545 (2020).
75. A. Pupo, A. Fernández, S. H. Low, A. François, L. Suárez-amarán, R. J. Samulski, AAV vectors : The Rubik's cube of human gene therapy. *Mol. Ther.* **30**, 3515–3541 (2022).
76. B. E. Maimon, M. Diaz, E. C. M. Revol, A. M. Schneider, B. Leaker, C. E. Varela, S. Srinivasan, M. B. Weber, H. M. Herr, Optogenetic peripheral nerve immunogenicity. *Sci. Rep.* **8**, 14076 (2018).
77. B. E. Maimon, K. Sparks, S. Srinivasan, A. N. Zorzos, H. M. Herr, Spectrally distinct channelrhodopsins for two-colour optogenetic peripheral nerve stimulation. *Nat. Biomed. Eng.* **2**, 485–496 (2018).

Acknowledgments: We thank I. Govindarajan for helping with mechanical design of the muscle characterization apparatus, E. Boyden for sharing confocal microscopy resources, C. Taylor and C. Varela for helpful advice and suggestions, and the Division of Comparative Medicine at MIT for help with animal work. **Funding:** This work was supported by K. Lisa Yang Center for Bionics at MIT and MIT Media Lab Consortia. G.H.-A. is supported by a K. Lisa Yang ICoN fellowship and a CONACYT doctoral fellowship. **Author contributions:** G.H.-A., H.S., and H.H. conceived and designed the experiments. G.H.-A. performed the surgeries and developed the muscle characterization apparatus. G.H.-A. and S.H.Y. developed the optical stimulator. G.H.-A. and H.S. developed the stimulation protocols and performed modeling. G.H.-A., H.S. and H.H. designed the controllers. G.H.-A., H.S., and S.G.-A. collected the data. G.H.-A., H.S., and O.G. analyzed the data. G.H.-A. and S.S. performed immunohistochemistry. H.H. supervised the work. G.H.-A. wrote the original manuscript. All authors reviewed and edited the manuscript. **Competing interests:** The authors declare that they have no competing interests. **Data and materials availability:** The data needed to evaluate the conclusions of this paper are in the main text, figures, and the Supplementary Materials. CAD files of the muscle characterization apparatus and code used for closed-loop control can be found at https://github.com/mitmedialab/Muscle-Optogenetics and https://zenodo.org/records/11061412.

Submitted 27 May 2023
Accepted 25 April 2024
Published 22 May 2024
10.1126/scirobotics.adi8995

Science Robotics

Closed-loop optogenetic neuromodulation enables high-fidelity fatigue-resistant muscle control

Guillermo Herrera-Arcos, Hyungeun Song, Seong Ho Yeon, Omkar Ghenand, Samantha Gutierrez-Arango, Sapna Sinha, and Hugh Herr

Sci. Robot. **9** (90), eadi8995. DOI: 10.1126/scirobotics.adi8995

Editor's summary

Electrical stimulation has been widely used in neuroprostheses to control and restore muscle function. However, this approach causes poor fine-force modulation and quickly leads to fatiguing of the muscles after brief stimulation. Herrera-Arcos *et al*. now present a closed-loop method for neuromodulation using optogenetics that alleviates the challenges associated with electrical stimulation. A biophysical model was also developed to understand the characteristics underlying neuromuscular optogenetic stimulation. They showed that functional optogenetic stimulation supported fatigue-resistant control of muscle with higher accuracy and higher generated force in vivo than electrical stimulation, demonstrating that it may potentially be adopted for prosthesis control. —Amos Matsiko